Above-threshold ionization in neon produced by combining optical and bichromatic XUV femtosecond laser pulses

Nicolas Douguet, Alexei N. Grum-Grzhimailo, and Klaus Bartschat

Phys. Rev. A **95**, 013407 — Published 19 January 2017

DOI: 10.1103/PhysRevA.95.013407

Above-threshold ionization in neon produced by combining optical and bichromatic XUV femtosecond pulses

Nicolas Douguet[1], Alexei N. Grum-Grzhimailo[2], and Klaus Bartschat[1]
[1] *Department of Physics and Astronomy, Drake University, Des Moines, Iowa 50311, USA and*
[2] *Skobeltsyn Institute of Nuclear Physics, Lomonosov Moscow State University, Moscow 119991, Russia*
(Dated: December 27, 2016)

We consider the ionization of neon induced by a femtosecond laser pulse composed of overlapping, linearly polarized bichromatic extreme ultraviolet and infrared fields. In particular, we study the effects of the infrared light on a two-pathway ionization scheme for which Ne $2s^2 2p^5 3s\,{}^1P$ is used as intermediate state. Using time-dependent calculations, supported by a theoretical approach based on the strong-field approximation, we analyze the ionization probability and the photoelectron angular distributions associated with the different sidebands of the ionization spectrum. Complex oscillations of the angular distribution anisotropy parameters as a function of the infrared light intensity are revealed. Finally, we demonstrate that coherent control of the asymmetry is achievable by tuning the infrared frequency to a nearby electronic transition.

PACS numbers: 32.80.Rm, 32.80.Fb, 32.80.Qk, 32.90.+a

I. INTRODUCTION

The coherent control of quantum phenomena by light [1, 2] stands at the heart of future promising developments in a variety of scientific areas. Manipulating two-pathway quantum interferences in atomic ionization is one way to achieve coherent control of the photoelectron angular distribution (PAD) (for example [3–7]). The principle consists of ionizing an atomic system using the fundamental and second harmonic of a short laser pulse, thereby producing two distinct ionizing pathways characterized by one-photon and two-photon absorption. The latter process, referred to below as $\omega + 2\,\omega$, was recently studied experimentally in the extreme ultraviolet (XUV) regime at the free-electron laser (FEL) FERMI in Trieste [8] using two color femtosecond (fs) pulses for the ionization of neon. The efficiency of the two-photon ionization pathway was enhanced by choosing one of the Ne $2p^5 4s$ states with total electronic angular momentum $J = 1$ as an intermediate stepping stone. Coherent control of the PAD asymmetry was achieved by varying the time delay, or the corresponding relative carrier envelope phase (CEP), between the two harmonics, to an unprecedented precision of 3.1 attoseconds. A description of the $\omega + 2\,\omega$ interference process in neon using $2p^5 3s$ as intermediate state is presented in Ref. [9].

In this paper we theoretically analyze the effect of an additional comparatively weak infrared (IR) field (Keldysh parameter $\gamma \gg 1$) on the $\omega + 2\,\omega$ ionization process and discuss the potential of the IR field to provide an additional degree of freedom to control the PAD.

The presence of the IR field ultimately leads to the well-known phenomenon of above-threshold ionization (ATI) [10–14], resulting in sidebands in the photoelectron spectrum associated with the absorption or stimulated emission of one or several IR photons [15–17]. Many studies, both experimental and theoretical, of the sideband patterns in XUV + IR ionization have been performed (for example [18–23]), including PADs of the sidebands [23–34]. Recently such experiments with circularly polarized XUV beams from FELs became feasible [35, 36].

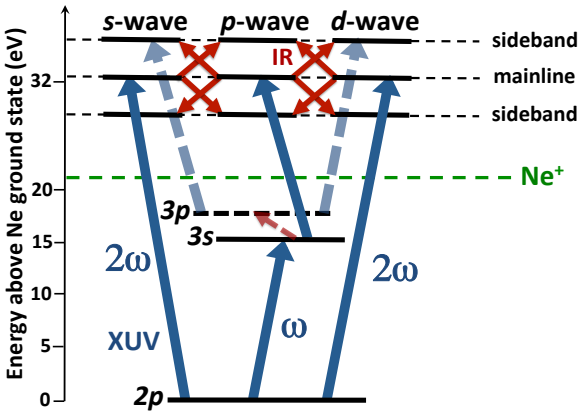

FIG. 1: Scheme of the $\omega + 2\,\omega + \Omega_0$ process in neon in the dipole approximation. The ionization is caused by the fundamental and second harmonic (solid blue arrows) of an XUV pulse whose fundamental frequency ω is tuned near the $2p \rightarrow 3s$ transition. The overlapping IR field induces ATI (small red arrows) transitions leading to sidebands in the spectrum. Only s, p, and d-waves are displayed, although higher partial waves can contribute. The dashed arrows represent additional paths created when the IR frequency is tuned near the $3s \rightarrow 3p$ transition (see text).

We chose neon as target for the study, because it is one of the atomic systems currently under investigation for coherent control experiments at the seeded FEL FERMI. We analyze ionization by a linearly polarized femtosecond pulse whose electric field, taken along the z-axis, is given by $\boldsymbol{\mathcal{E}}(t) = \boldsymbol{\mathcal{E}}_X(t) + \boldsymbol{\mathcal{E}}_{IR}(t)$, where the XUV and IR com-

ponents of the field are

$$\mathcal{E}_X(t) = \bar{\mathcal{E}}_X f(t)[\cos(\omega t) + \eta_X \cos(2\omega t + \varphi_X)], \quad (1)$$
$$\mathcal{E}_{IR}(t) = \eta_0 \bar{\mathcal{E}}_X f(t) \cos(\Omega_0 t + \varphi_0). \quad (2)$$

In the above equations, $f(t)$ is a smoothly varying pulse envelope, common to both XUV and IR fields, Ω_0 is the infrared frequency, φ_X and φ_0 are the CEPs of the second harmonic and the IR field, respectively, while the parameters η_X and η_0 characterize their relative strength with respect to the fundamental amplitude $\bar{\mathcal{E}}_X$. In our case the XUV pulse contains many optical cycles. Hence the CEP of the fundamental frequency ω in Eq. (1) is unimportant, and we set it to zero.

The ionization scheme of the $\omega + 2\,\omega + \Omega_0$ process is presented in Fig. 1. We use the single active electron (SAE) approximation to label neon electronic states, and the dipole approximation is employed throughout this study. The scheme consists of tuning the fundamental frequency near the $2p^6\,{}^1S_0 \rightarrow 2p^5 3s\,{}^1P_1$ excitation energy of neon, which is associated with the one-electron transition $2p \rightarrow 3s$. This results in a resonant two-photon ionization pathway, which produces mostly p-wave photoelectrons. On the other hand, the second harmonic ionizes neon via nonresonant one-photon absorption, producing s-wave and d-wave photoelectrons. These distinct pathways produce photoelectrons with partial waves of different parity, thereby leading to an asymmetric PAD.

The superimposed IR field creates equally spaced sidebands around the mainline (ML). This is illustrated in Fig. 2 for an IR frequency $\Omega_0 = 0.55$ eV. The sidebands are labeled as $\mathrm{SB}_{\pm n}$ according to the minimum number of IR photons absorbed or emitted in the ATI process, and $n > 0$ is the band order. By definition, ML is the 0^{th} order band.

Although only s, p, and d-waves are shown in Fig. 1, higher partial waves also contribute increasingly with higher IR intensity. The differences in the relative contributions of partial waves lead to distinct PADs at the different sidebands. Such dissimilarities may become particularly pronounced in the extreme situation where the IR frequency is tuned to a nearby electronic state. Such a situation is shown in Fig. 1 when the IR frequency is set in resonance with the $3s \rightarrow 3p$ one-electron transition, thus creating a pathway to ML and enhancing a "non-ATI" pathway for ionization towards the lowest high-energy sideband. As will be shown below, this pathway can provide additional control on the PADs at different electron kinetic energies.

The weak field ($\eta_0 \ll 1$) characteristics of the different sidebands can be obtained from lowest-order perturbation theory [37, 38]. Describing the process at larger intensities requires further expansion of the ionization amplitude into a Born series including higher-order terms. However, such an expansion would necessitate the computation of free-free transition dipole moments, which are notoriously difficult to evaluate [39–41]. On the contrary, the Keldysh-Faisal-Reiss theory [42–45] in the strong-field approximation (SFA) can be used to evaluate characteristics of the ionization amplitude at the different sidebands, as recently demonstrated by Kazansky *et al.* [46] and also described by Bauer [47, 48] for strong-field photoionization by a circularly polarized laser field. Therefore, we use the SFA to describe the ATI process in the following development.

The next section provides a description of the numerical approach employed to solve the time-dependent Schrödinger equation (TDSE) and the SFA theoretical framework. In Sec. III, we present our theoretical and numerical results and discuss the principal outcomes of the study. Section IV is devoted to our conclusions.

Unless otherwise indicated, atomic units are used throughout this manuscript.

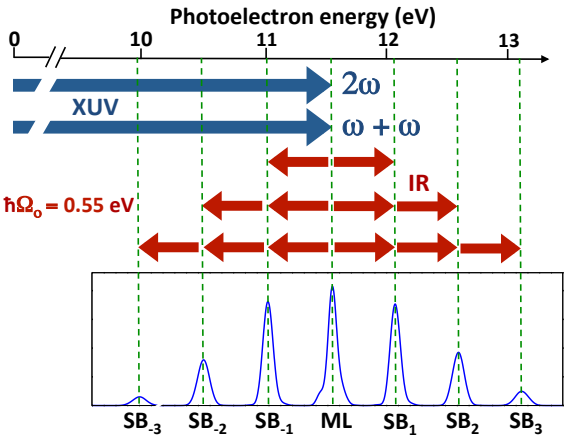

FIG. 2: Example of a photoelectron spectrum showing the different sidebands associated with the minimum number of absorbed or emitted photons.

II. THEORY

Within the dipole approximation, the PAD is axially symmetric with respect to the direction of linear polarization and is of the general form

$$\frac{dW}{d\Omega} = \frac{W_0}{4\pi}\left[1 + \sum_{k=1}^{\infty} \beta_k P_k(\cos\theta)\right], \quad (3)$$

where $d\Omega$ represents the solid-angle element for a photoelectron emitted into the direction defined by (θ, ϕ), W_0 is the angle-integrated ionization probability, $P_k(\cos\theta)$ are Legendre polynomials, and β_k are anisotropy parameters. Although not explicitly shown in Eq. (3), the angular distribution, ionization probability, and anisotropy parameters depend on the electron kinetic energy ε. One can obtain anisotropy parameters associated with a given band by computing their averaged value $\mathcal{P}^{-1}\int \beta_k W_0 d\varepsilon$ over the energy range spanned by the band, with its ionization probability given by $\mathcal{P} = \int W_0 d\varepsilon$.

The left-right asymmetry is defined as

$$A(0^\circ) = \frac{W(0^\circ) - W(180^\circ)}{W(0^\circ) + W(180^\circ)}, \tag{4}$$

where $W(\theta)$ is the ionization signal in the θ direction. The left-right asymmetry can readily be expressed in terms of the anisotropy parameters as [49]

$$A(0^\circ) = \frac{\sum_{k=0}^{\infty} \beta_{2k+1}}{1 + \sum_{k=1}^{\infty} \beta_{2k}}. \tag{5}$$

One clearly sees that only the odd-rank anisotropy parameters are responsible for the asymmetry of the PAD. In second-order time-dependent perturbation theory (PT), the PAD (3) is expressed as

$$\frac{dW}{d\Omega} = \sum_{M_f=0,\pm1} |U^{(1)}_{\boldsymbol{k},M_f} + U^{(2)}_{\boldsymbol{k},M_f}|^2, \tag{6}$$

where we introduced the first- and second-order ionization amplitudes for a photoelectron with asymptotic momentum $\boldsymbol{k}$. In Eq. (6), the residual ion has orbital angular momentum $L_f = 1$ and magnetic quantum number M_f. Here we limit our consideration to an atom with zero initial angular momentum.

In the following we employ the approach of [46, 50] to develop the SFA for the $\omega + 2\,\omega + \Omega_0$ process, however, we use the Coulomb-Volkov (CV) approximation [51–54]. The first-order ionization amplitude for one XUV photon absorption with the electronic wave function "dressed" in the IR field takes the form

$$U^{(1)}_{\boldsymbol{k},M_f} = -i \int_0^{t_M} \mathcal{E}_X(t) \langle \Psi_f \psi^{CV}_{\boldsymbol{k}} \,|\, \hat{d}_z \,|\, \Psi_0 \rangle e^{-i\varepsilon_{2p}t} dt\,, \tag{7}$$

where $\varepsilon_{2p} < 0$ is the binding energy of the $2p$ electron and t_M indicates the end of the pulse that started at $t = 0$. Furthermore, $\hat{d}_z = \sum_j z_j$ is the component of the electric dipole operator, where the sum is taken over all atomic electrons, Ψ_0 is the neon ground state, Ψ_f is the final ionic state of Ne^+, and $\psi^{CV}_{\boldsymbol{k}}$ denotes the Coulomb-Volkov wave function [52]:

$$\psi^{CV}_{\boldsymbol{k}}(\boldsymbol{r}) = \varphi^-_{\boldsymbol{k}}(\boldsymbol{r}) \exp\left(i\boldsymbol{A}(t)\cdot\boldsymbol{r} - \frac{i}{2}\int_\infty^t dt' [\boldsymbol{k} + \boldsymbol{A}(t')]^2 \right). \tag{8}$$

In the above equation, $\boldsymbol{A}(t) = \int_t^\infty \boldsymbol{\mathcal{E}}_{IR}(t')\,dt'$ is the vector potential of the IR field while $\varphi^-_{\boldsymbol{k}}$ is an incoming eigenstate of the field-free SAE Hamiltonian. Since in the present situation $k \gg A(t)$, and $\boldsymbol{A}(t)\cdot\boldsymbol{r} \ll 1$ over the extent of the $2p$ orbital of neon, we can approximate $\varphi^-_{\boldsymbol{k}}(\boldsymbol{r}) \exp(i\boldsymbol{A}(t)\cdot\boldsymbol{r}) \approx \varphi^-_{\boldsymbol{k}}(\boldsymbol{r})$ in (8) when evaluating (7). Within the single-configuration model, the matrix element in (7) is reduced to a one-electron matrix element. Expanding the continuum function $\varphi^-_{\boldsymbol{k}}$ in partial waves and considering the electron initially in a p-orbital, the amplitude (7) can be cast into the form

$$U^{(1)}_{\boldsymbol{k},M_f} = -i\left[\mathcal{A}^{(1)}_{\varepsilon s,m} \mathcal{F}_{s,m}(\boldsymbol{k}) + \mathcal{A}^{(1)}_{\varepsilon d,m} \mathcal{F}_{d,m}(\boldsymbol{k}) \right], \tag{9}$$

where $m = -M_f$,

$$\mathcal{F}_{\ell,m}(\boldsymbol{k}) = \eta_X \bar{\mathcal{E}}_X \int_0^{t_M} dt\, f(t) Y_{\ell m}(\theta,\phi) \times \exp\left[-i\int_t^\infty dt' \left(\frac{1}{2}[\boldsymbol{k} + \boldsymbol{A}(t)]^2 - (2\,\omega + \varepsilon_{2p}) \right) \right], \tag{10}$$

$Y_{\ell m}(\theta,\phi)$ are spherical harmonics, and

$$\mathcal{A}^{(1)}_{\varepsilon\ell,m} = i^{-\ell} e^{i\delta_\ell} \langle \varepsilon \ell m \,|\, z \,|\, 2p, m \rangle\,. \tag{11}$$

Here we separated out the phase factor $i^{-\ell}e^{i\delta_\ell}$ from the continuum wavefunction with δ_l as the scattering (potential plus Coulomb) phase, $\varepsilon = k^2/2$ is the asymptotic electron energy, and (θ,ϕ) are the detection angles associated with $\boldsymbol{k}$.

The integral in brackets of Eq. (10) can be evaluated analytically for an infinitely long "pulse" (steady-state excitation) [46], i.e., assuming that $f(t)$ is a smooth function, equal to unity for most time, and tending to zero for $t \to \infty$, such that $A(t) \approx -\left(\eta_0 \bar{\mathcal{E}}_X/\Omega_0\right) \sin(\Omega_0 t + \varphi_0)$. Neglecting the term proportional to A^2 in (10) and using the Jacobi-Anger expansion, one obtains

$$\mathcal{F}_{\ell,m}(\boldsymbol{k}) = \eta_X \bar{\mathcal{E}}_X \sum_{n=-\infty}^{\infty} i^n J_n(q) e^{-i(\varphi_X + n\varphi_0)} \times \int_0^{t_M} dt\, f(t) Y_{\ell m}(\theta,\phi) e^{i(\varepsilon - \varepsilon_n)t}\,, \tag{12}$$

where $\varepsilon_n = 2\,\omega + \varepsilon_{2p} + n\Omega_0$, $q = (\eta_0 k A/\Omega_0)\cos\theta$, $J_n(q)$ is the n^{th} Bessel function of the first kind. Rearranging the terms in the sum we obtain (for $\ell = 0$ and $\ell = 2$)

$$\mathcal{F}_{\ell,m}(\boldsymbol{k}) = \sum_{n=-\infty}^{\infty} \mathcal{F}^{(n)}_{\ell,m}(\boldsymbol{k}) T^{(1)}_n\,, \tag{13}$$

with

$$\mathcal{F}^{(n)}_{\ell,m}(\boldsymbol{k}) = i^n J_n(q) Y_{\ell m}(\theta,\phi)\,, \tag{14}$$

and in the rotating-wave approximation,

$$T^{(1)}_n = \eta_X \bar{\mathcal{E}}_X e^{-i(\varphi_X + n\varphi_0)} \int_0^{t_M} f(t) e^{i(\varepsilon - \varepsilon_n)t} dt\,. \tag{15}$$

The process of two-photon resonant absorption is dominated by the pathway $2p \to 3s \to \varepsilon p$, thus producing a p-wave photoelectron with $m = 0$. Therefore, we neglect the contribution of other intermediate states. The second-order ionization amplitude is deduced from similar considerations and takes the form

$$U^{(2)}_{\boldsymbol{k},M_f} = i^2 \mathcal{A}^{(2)}_{\varepsilon p,m} \mathcal{F}_{p,m}(\boldsymbol{k}), \tag{16}$$

where

$$\mathcal{F}_{p,m}(\boldsymbol{k}) = \sum_{n=-\infty}^{\infty} \mathcal{F}^{(n)}_{p,m}(\boldsymbol{k}) T^{(2)}_n, \tag{17}$$

with

$$T_n^{(2)} = \bar{\mathcal{E}}_X^2 e^{-in\varphi_0} \int_0^{t_M} f(t) e^{i(\varepsilon-\varepsilon_n-\Delta\omega)t} \int_0^t f(t') e^{i\Delta\omega t'} dt', \tag{18}$$

where $\Delta\omega = \varepsilon_{3s} - \varepsilon_{2p} - \omega$ and

$$\mathcal{A}^{(2)}_{\varepsilon p,m} = \delta_{m,0}\, i e^{i\delta_p} \langle \varepsilon p, m \,|\, z \,|\, 3s, m\rangle \langle 3s, m \,|\, z \,|\, 2p, m\rangle. \tag{19}$$

If the XUV pulse contains many cycles, the functions $T_n^{(1)}$ and $T_n^{(2)}$ will be narrow peaks centered at the energy position ε_n of SB_n, turning into a δ-function in the limit of continuous radiation. Consequently, one can describe the ionization at SB_n by ignoring all terms but $\mathcal{F}^{(n)}_{\ell,m}(\boldsymbol{k})$ in Eqs. (13) and (17).

Note that the CEP φ_0 is factored out as $\exp[in\varphi_0]$ in the total photoionization amplitude into the SB_n sideband (see Eqs. (15) and (18)). Therefore, the observable quantities do not depend on the CEP of the overlapping IR pulse. This feature was confirmed to high accuracy by our numerical calculations. It is an important property since, in contrast to the relative CEP φ_X between the XUV harmonics, which can be experimentally controlled to high precision [8], φ_0 is hardly controllable and mostly chaotic. Hereafter, we set $\varphi_0 = 0$.

Using Eq. (6) and collecting Eqs. (7), (13), (14), (16), and (17), we obtain the angular distribution at SB_n and ML in the form

$$\begin{aligned}\frac{dW^{(n)}}{d\Omega} &= J_n^2(q)\Big(\Big|\mathcal{A}^{(1)}_{\varepsilon s,0} Y_{00}(\theta,\phi) T_n^{(1)} \\ &\quad + \mathcal{A}^{(1)}_{\varepsilon d,0} Y_{20}(\theta,\phi) T_n^{(1)} - i\mathcal{A}^{(2)}_{\varepsilon p,0} Y_{10}(\theta,\phi) T_n^{(2)}\Big|^2 \\ &\quad + 2\Big|\mathcal{A}^{(1)}_{\varepsilon d,1} Y_{21}(\theta,\phi) T_n^{(1)}\Big|^2\Big) \qquad (20) \\ &\approx J_n^2(q) \frac{dW^{(0)}}{d\Omega} \qquad (21)\end{aligned}$$

The form (21) is typical for the SFA within the "soft-photon approximation" [23] (see also [36]). The ionization probability and anisotropy parameters at SB_n are, respectively, given by

$$W^{(n)} = \int \frac{dW^{(n)}}{d\Omega} d\Omega\,, \tag{22}$$

$$\beta_k^{(n)} = \frac{2k+1}{W^{(n)}} \int \frac{dW^{(n)}}{d\Omega} P_k(\cos\theta) d\Omega. \tag{23}$$

In the limit $\eta_0 \to 0$, calculating $\beta_k^{(0)}$ in Eq. (23) and using $J_0(0) = 1$, one can recover the lowest-order PT expressions for the anisotropy parameters (see Eqs. (7)−(11) of Ref. [9]), when including only the contribution from the $3s$ intermediate state.

The elements $\mathcal{A}^{(i)}_{\ell,m} T_n^{(i)}$, $i = 1, 2$ in Eq. (20) are extracted below from the ionization amplitude computed in the TDSE approach in the absence of the IR field. The latter elements carry information on the $\omega + 2\,\omega$ process at ML for $\eta_0 = 0$, while the SFA predicts the effect of the IR field on the characteristics of the different bands (ML + $\mathrm{SB}_{\pm n}$) as a function of η_0.

The general procedure to numerically solve the TDSE for linearly polarized electric field was described at length in Ref. [56] for the case of atomic hydrogen. For a multi-electron system, similar to [9], we solve the TDSE using the SAE approximation in an averaged electronic potential computed to reproduce as accurately as possible the energy levels of the neon excited states. The $2p \to 3s$ excitation energy and the neon ionization energy obtained in our potential are, respectively, 16.36 eV and 21.16 eV in the SAE approach, whereas the experimental values are 16.85 eV and 21.56 eV [57, 58]. The fine-structure splitting between the atomic states is not included in our nonrelativistic approach. Since the LS-purity of the $\mathrm{Ne}(2p^5 3s)^1P_1$ state is about 93% [59], we neglect the ^{3}P component of this configuration. In this case, the SAE model should work reasonably well.

In the SAE approximation, the one-electron wavefunction is initially propagated from the $(2p, m)$ orbital of neon. At the end of the pulse, the wavefunction is projected onto continuum distorted-wave functions of Ne^+. All physical observables, such as the ionization probability and the PAD with its associated anisotropy parameters, can then be computed in a straightforward way. In order to represent an unpolarized atomic target, we propagated the three projections of the initial angular momentum m of the $2p$ orbital independently and subsequently average the results. We included $\ell \leq 14$ in order to ensure the numerical convergence of our predictions.

III. RESULTS AND DISCUSSION

The numerical simulations in this work were performed using pulse envelopes of the form $f(t) = \sin^2 \Omega t$ ($\Omega = \omega/2N, 0 \leq t \leq t_M$), where N is the number of XUV cycles. Hereafter, we take a pulse with $N = 300$ cycles, corresponding to a FWHM of the intensity ~ 27 fs. The amplitude ratio $\eta_X = 0.1$ is fixed at a value producing a significant $\omega + 2\,\omega$ interference. The intensity of the fundamental is chosen relatively low, $10^{12}\mathrm{W/cm}^2$, to ensure the applicability of the PT approach in describing the $\omega + 2\,\omega$ process.

In order to minimize processes involving absorption or emission of IR photons prior to ionization, we choose a low IR frequency, $\Omega_0 = 0.55$ eV (corresponding to $\approx 2.25\,\mu$m) in the mid-infrared range. The IR field spans $N_0 = 10$ cycles in order to completely overlap with the XUV pulse. For such a low IR frequency, pathways of the form $\hbar\omega \pm \hbar\Omega_0 + \hbar\omega$ have a negligible effect, since no intermediate bound states are reachable by less than the absorption or emission of four IR photons. Multiphoton ionization of the form $\hbar\omega + n\hbar\Omega_0$ is also an inefficient process at such low IR intensity, because the system should absorb $n \geq 9$ photons to ionize from the $3s$ state.

A. General Appearance of Sidebands

The angle-integrated photoelectron spectra computed in the TDSE approach are shown in Fig. 3 at different amplitude ratios η_0. Without the IR field, only ML appears in the spectrum. As the IR intensity is increased, $SB_{\pm 1}$ are first created as a result of a single IR photon emission or absorption. Turning to larger intensities, $SB_{\pm n}$ with $n \geq 2$ appear as a consequence of multiphoton processes. The general tendencies for variations of the spectrum in the XUV + IR ionization are well established and are directly applicable in our case of $\omega+2\omega+n\Omega_0$ ionization, since the interference between the amplitudes of even-photon and odd-photon ionization vanishes in the angle-integrated photoelectron spectra. The ionization probability redistribution, and its dependence as a function of the IR field intensity, can be successfully modeled by the SFA approach [23]. For $\eta_0 \geq 0.3$, nearby sidebands acquire an additional structure, which actually becomes a "double-peak" at higher intensities. Its origin can be attributed to the ponderomotive energy and AC Stark shifts [60–63].

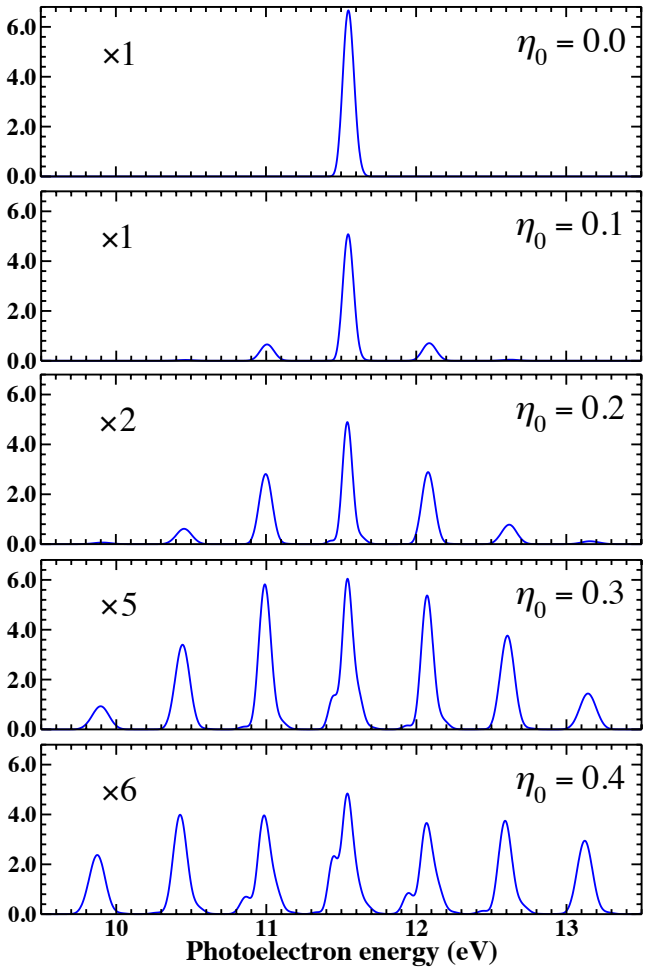

FIG. 3: TDSE results for the ionization probability (in units of 10^{-3}eV^{-1}) as a function of the photoelectron energy for different IR field amplitude ratios η_0. The fundamental XUV intensity is $I = 10^{12}\text{W/cm}^2$, $\eta_X = 0.1$, and the infrared frequency is $\Omega_0 = 0.55$ eV.

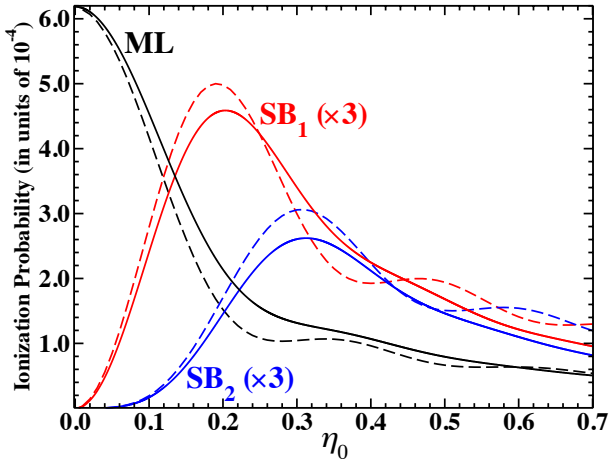

FIG. 4: Ionization probability associated with the different bands calculated in the TDSE (solid lines) and the SFA (dashed lines) approaches as a function of the IR field amplitude ratio η_0.

In the present study, we focus on the characteristics of ML and SB_n for $|n| \leq 2$. Since SB_n and SB_{-n} are formed, for small n, from approximately the same transition matrix elements, they exhibit similar characteristics within negligible differences. Thus, we will only show results for ML, SB_1 and SB_2 in the following development. Similar results would be found for SB_{-1} and SB_{-2}, respectively.

The ionization probability associated with the different bands is presented in Fig. 4 as a function of η_0. Since at high IR intensity the spectrum becomes strongly distorted, we only show the results for $\eta_0 \leq 0.7$. The TDSE predictions are compared with the SFA results obtained using Eqs. (20) and (22). Overall good agreement is obtained between the two sets of results. Ionization at ML decreases monotonically with growing η_0, whereas the weak-field ionization of SB_1 and SB_2 increases as η_0^2 and η_0^4, respectively, in accordance with lowest-order (non-vanishing) PT predicting an η_0^{2n} dependence. However, as the IR intensity is increased, the validity of PT breaks down rapidly. The ionization probability in the sidebands reaches a maximum and gradually decreases as a function of intensity. The positions of the maxima of SB_1 and SB_2 at $\eta_0 \approx 0.2$ and $\eta_0 \approx 0.3$, respectively, are similar in the TDSE and SFA results. On the other hand, oscillations predicted by the SFA are hardly apparent in the TDSE calculations.

B. Angular Distribution of Sidebands

Calculations of the anisotropy parameters β_k for $k \leq 6$ as function of η_0 in the TDSE and SFA approaches are

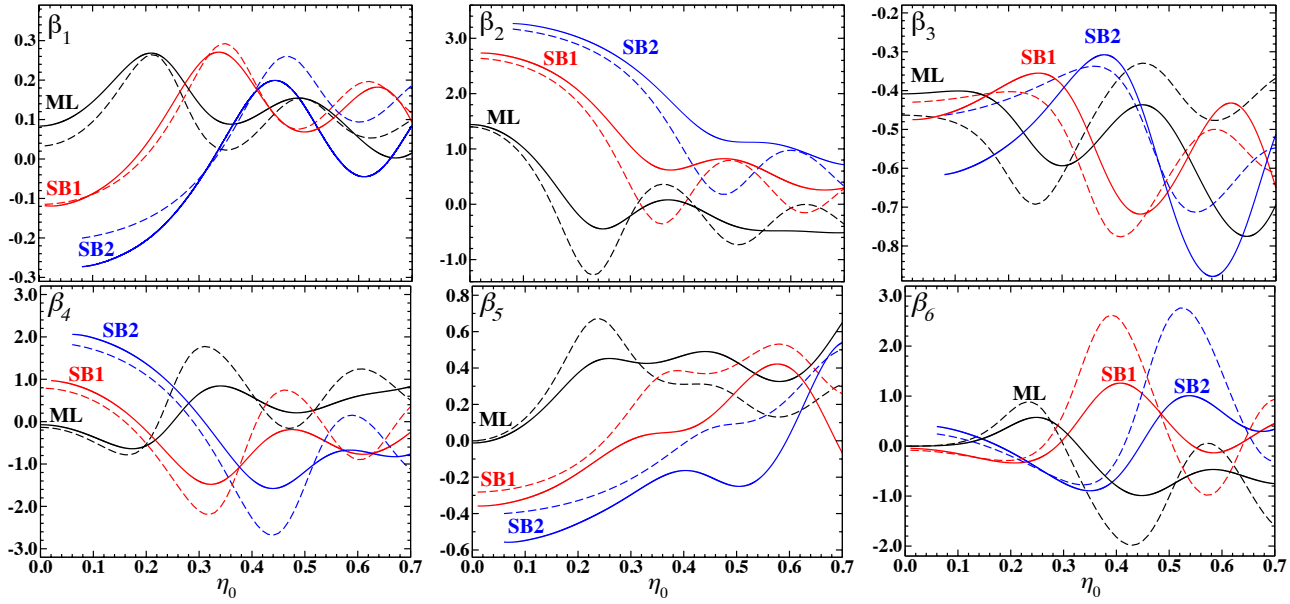

FIG. 5: Anisotropy parameters β_k ($1 \le k \le 6$), for $\varphi_X = 0$, as a function of the IR field amplitude ratio η_0. The labels are the same as in Fig. 4.

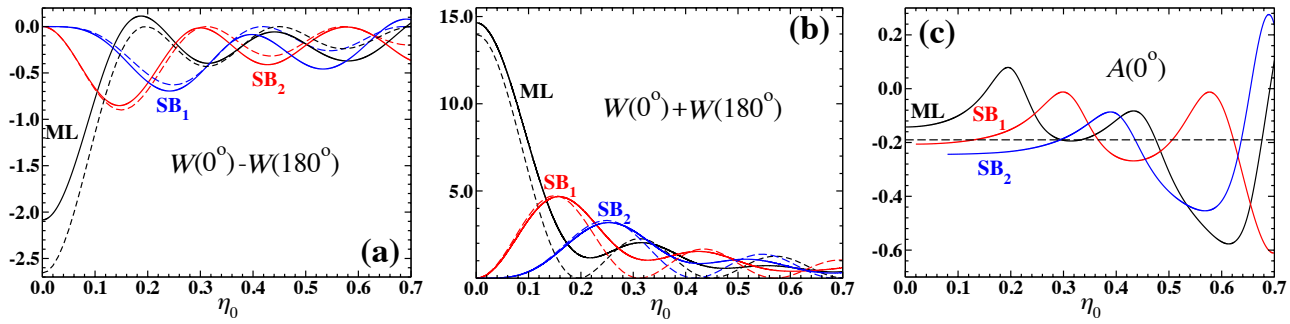

FIG. 6: Subtracted (a) and summed (b) forward and backward ionization probability signals (in units of 10^{-4}), as well as the left-right asymmetry (c), as a function of the IR field amplitude ratio η_0, as calculated in the TDSE and SFA approaches. Note the constant value of $A(0^\circ)$ in the SFA.

depicted in Fig. 5. A first prominent feature consists of nonzero values of odd-rank β_k, which are the result of interference between ionization paths involving even and odd numbers of photons. Interestingly, for weak IR fields, the absolute values of odd-rank β_k systematically increase with increasing n. The ML anisotropy parameters β_5 and β_6 vanish at $\eta_0 = 0$, because only one- and two-photon absorption can occur at the ML in the absence of an IR field. Note also that β_4 associated with ML is zero without an IR field in a simplified version of the second-order PT with only one resonant $3s$ intermediate state. Since SB_1 and SB_2 are, respectively, formed from absorption of at least one XUV and one or two additional IR photons, they exhibit nonvanishing values of β_5 and β_6 as long as the sidebands can be seen at small η_0. The good agreement between TDSE and SFA at ML for $\eta_0 = 0$ is not surprising since the parameters in Eq. (20) were extracted from the TDSE code in the absence of IR field. The small remaining discrepancies, apparent for β_1 and β_3, are due to the fact that the PT only includes s, p, and d-waves, whereas more partial waves are included in the TDSE calculations.

The results from both calculations, TDSE and SFA, clearly exhibit oscillations, although their amplitudes are significantly larger in the SFA approach. Nevertheless, the positions of the maxima and minima, the sign of curvatures, and the limiting values of the anisotropy parameters for $\eta_0 \ll 1$ are in correspondence in the two approaches. These oscillations should be experimentally observable. Similar oscillations in $\beta_2^{(1)}$ and $\beta_4^{(1)}$ were obtained within SFA [36] for ionization of helium by circularly polarized XUV and IR radiation. Such a complicated intensity dependence is determined by the interplay

of Bessel functions, weighted by the Legendre polynomials, and the denominator in expression (23). Within the TDSE approach, the oscillations are due to the contribution of many partial waves originating from absorption and emission of multiple photons.

The origin of the discrepancies between the TDSE and SFA results can be attributed to several factors. First, the SFA approach neglects the dynamical atomic polarizability, which becomes important at strong IR fields and should perturb the two-photon pathway through the AC-Stark shifted $3s$ state. More importantly, in the SFA, it is assumed that the field is stationary ($N \to \infty$), whereas the pulse used in the TDSE calculations is still relatively short with $N = 300$ cycles. The fact that the pulse envelope $f(t)$ is different in the SFA and TDSE models might explain most of the observed discrepancies. In addition, for large $\eta_0 \geq 0.4$, the absorption of four photons is likely to occur (see Fig. 3). In this situation, intermediate bound states, and even Rydberg states, might play a significant role in the ionization process, however, they are not accounted for in the SFA approach.

It is interesting to evaluate the variation of the left-right asymmetry $A(0°)$, Eq. (4), as a function of the IR intensity, since it is an indicator for interference between the amplitudes of odd-photon and even-photon ionization. Figures 6(a,b) compare the subtracted and summed right ($\theta = 0$) and left ($\theta = \pi$) emission probabilities calculated in the TDSE and SFA approaches. To obtain converged results at large IR intensity, we included anisotropy parameters β_k up to $k \leq 24$. The TDSE and SFA results agree reasonably well over the intensity range covered. On the other hand, the asymmetries (Fig. 6(c)), i.e., the relative difference between these results, behave differently in each approach as function of the IR field amplitude ratio η_0. In the SFA, the asymmetry is predicted to have a constant value independent of both the band and the IR intensity. This feature is inherent to the SFA and follows directly from Eq. (21); the electron in the IR field carries any initial asymmetry created in the ML ($n = 0$) by the $\omega + 2\,\omega$ process over to the different sidebands. On the contrary, the TDSE results exhibit oscillations of the asymmetry whose amplitude increases as a function of the relative IR intensity.

Additional information on the asymmetry can be obtained by analyzing its variation as a function of the relative CEP between the harmonics. The left-right asymmetry $A_n(\eta_0, \varphi_X) = a_n(\eta_0)\cos[\varphi_X + \varphi_n(\eta_0)]$ at each band has a sinusoidal form, where (at fixed η_X) the functions $a_n(\eta_0)$ and $\varphi_n(\eta_0)$ depend on the IR intensity only. The variation of the asymmetry as a function of the relative CEP at $\eta_0 = 0.2$ is presented in Fig. 7(a). Although the amplitude of the oscillations is about 30-40% larger for SB_1 and SB_2 than for ML, the phase-shift $\varphi_n \leq 0.5$ rad remains small. Consequently, the asymmetry at the different sidebands depicts close-lying values at all values of φ_X. Experimentally, this means that an independent control of the asymmetry at the different bands as a function of the relative CEP and IR intensity might only be possible for sufficiently short pulses, while only a common control of all bands can be achieved for long pulses.

C. Coherent Control of the Sidebands

The asymmetry is known to strongly vary in situations when one of the pathways involves an intermediate resonance. Varying the XUV fundamental frequency near the intermediate $3s$ state leads to a Fano-like profile of the asymmetry at ML [9, 49], which would be transferred to the sidebands by a sufficiently long IR pulse. To produce a selected control of the bands' asymmetry, an additional resonant path with nonequivalent effects on the different bands should be created. Such a scheme could be realized by creating an ionizing path different from $\omega + 2\,\omega$, for example by tuning the IR frequency near the $3s \to 3p$ transition ($\Omega_0 = 1.88$ eV in the SAE model), as shown in Fig 1. The PAD associated with SB_1 is then expected to strongly reflect the opening of the new pathway. Since our SFA model cannot take into account the $3s \to 3p$ transition, we only present TDSE predictions below.

Results for the asymmetry at ML and SB_1 as a function of the IR frequency are presented for $\eta_0 = 0.2$ and $\eta_0 = 0.3$ in Fig. 7(b). The onset in that panel shows the spectrum at $\Omega_0 = 1.88$ eV for an IR field covering

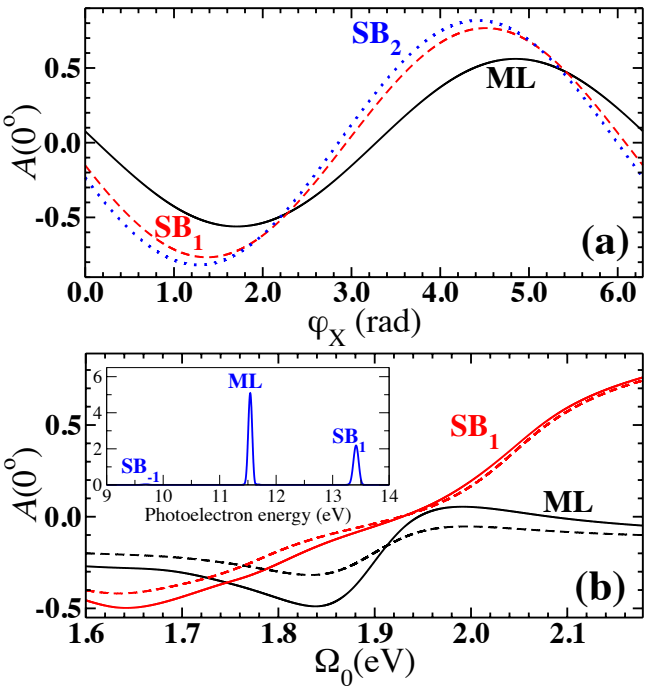

FIG. 7: (a) Left-right asymmetry $A(0°)$ for ML (black solid line), SB_1 (red dashed line) and SB_2 (blue dotted line), as a function of φ_X at $\Omega_0 = 0.55$ eV and $\eta_0 = 0.2$. (b) Left-right asymmetry $A(0°)$ as a function of the IR frequency Ω_0 at $\eta_0 = 0.2$ (dashed lines) and $\eta_0 = 0.3$ (solid lines). The inset shows the corresponding ionization probability spectrum (in units of 10^{-3} eV^{-1}) at $\eta_0 = 0.3$.

$N_0 = 30$ cycles to overlap with the XUV pulse at this frequency. Since one can barely see SB_{-1} and only the signals at ML and SB_1 are visible for the chosen pulse parameters, we present the asymmetry at just ML and SB_1.

The asymmetry at SB_1 exhibits a broad and steady increase, starting from about -0.45 at $\Omega_0 = 1.60$ eV and ending at almost 0.80 at $\Omega_0 = 2.20$ eV. As seen in Fig. 7(b), this variation depends only weakly on the IR intensity, as opposed to the asymmetry at ML, which clearly shows an asymmetric resonance profile whose amplitude increases as a function of the IR intensity. We have checked that the asymmetry remains the same to negligible differences if one uses a gaussian instead of a sine-squared envelope. The cause of the resonance profile at ML is actually indirect: as the IR frequency Ω_0 approaches the resonance, a transfer of population from $3s \to 3p$ occurs, thereby decreasing the two-photon ionization pathway and ultimately modifying the value of the asymmetry. Consequently, one can control the asymmetry amplitudes by varying the IR intensity and frequency. The latter effect could, for instance, be exploited experimentally to control the resonance profile without having to vary the amplitude ratio between the XUV harmonics, which is a difficult task to achieve in practice. Nevertheless, a complication arises in the present situation due to the fact that the system only needs to absorb two IR photons to ionize from the $3p$ excited state of neon. As a result, near-threshold ionization might become important for large IR intensities and could hinder good statistics of the experimental data. Thus, it seems preferable to use this scheme on a more strongly bound electronic state, for which multiphoton ionization would remain negligible.

Finally, note that for large IR frequencies in Fig. 7(b), the asymmetries in ML and SB_1 differ significantly. It might then be possible, by appropriately varying φ_X, to create a situation when the asymmetries of ML and SB_1 have opposite signs, i.e., a situation in which electrons of two different lines have opposite preferred emission directions with a resolvable energy difference. This strong difference in the asymmetry between ML and SB_1 contradicts the SFA prediction. The difference is most probably due to the $\hbar\omega + \hbar\Omega_0 + \hbar\omega$ and $\hbar\omega + 2\hbar\Omega_0 + \hbar\omega - \hbar\Omega_0$ pathways to SB_1, which cannot be adequately described in the SFA approach.

IV. CONCLUSION

We have presented a detailed investigation of above-threshold ionization effects induced by an infrared field on two-pathway interference between a nonresonant one-photon and resonant two-photon ionization of neon. The characteristics of the sidebands in the photoelectron spectrum were analyzed at several infrared laser intensities by numerically solving the time-dependent Schrödinger equation. The numerical results were qualitatively supported by analytical formulas derived from a model based on the strong-field approximation.

The ionization probability and the anisotropy parameters characterizing the angular distribution at each band agree well with each other in both models. The anisotropy parameters of the photoelectron angular distribution exhibit oscillations, which should be measurable experimentally.

An important result of our study is that for long pulses the left-right asymmetry at each sideband should not depart strongly from the asymmetry created at the main photoelectron line in the absence of infrared field. As the infrared intensity is increased, variations of the asymmetry are shown to become significant for relatively strong fields, where the ionization signal at each band should be harder to detect. In fact, in the strong-field approximation, the asymmetry is predicted to be constant, independent of the sideband order and the infrared pulse intensity, i.e., the infrared field transfers the asymmetry of the main photoelectron line to the different sidebands.

An interesting situation may occur if the infrared frequency is set in resonance with a nearby optically allowed electronic state. In such a case, the infrared field can play an active role in the ionization process. We have shown that the pumping of population from $3s$ to $3p$ results in a resonance profile of the asymmetry at the mainline as a function of the infrared frequency. Furthermore, the amplitude of the resonance profile at the main line increases with growing infrared intensity. The asymmetry of the lowest high-energy band exhibits the most interesting variation, since it changes significantly with the infrared frequency in a monotonic fashion. On the other hand, it merely varies as a function of the infrared intensity. Initial experiments to reveal some of the features provided by the infrared field were already performed at the FERMI free-electron laser facility in Trieste (Italy), and future experiments could use such effects to improve control of the photoelectron angular distribution.

Acknowledgments

The authors benefited greatly from stimulating discussions with Giuseppe Sansone, Michael Meyer, Elena Gryzlova, and Nikolay Kabachnik. The work of N.D. and K.B. was supported by the United States National Science Foundation under grant No. PHY-1430245 and the XSEDE allocation PHY-090031. The calculations were performed on SuperMIC at the Center for Computation & Technology at Louisiana State University.

[1] M. Shapiro and P. Brumer, J. Chem. Phys. **84**, 4103 (1986).

[2] P. Brumer and M. Shapiro, *Principles of the Quan-*

tum Control of Molecular Processes (Wiley-VCH, Berlin, 2003).
[3] N.B. Baranova, I. M. Beterov, B. Ya. Zel'dovich, I. I. Ryabtsev, A. N. Chudinov, and A. A. Shul'ginov, Pis'ma Zh. Eksp. Teor. Fiz. **55**, 431 (1992) [JETP Lett. **55**, 439 (1992)].
[4] Y.-Y. Yin, C. Chen, D. S. Elliott, and A. V. Smith, Phys. Rev. Lett. **69**, 2353 (1992).
[5] K. J. Schafer and K. C. Kulander, Phys. Rev. A **45**, 8026 (1992).
[6] E. Ehlotzky, Phys. Rep. **345**, 175 (2001).
[7] V. A. Astapenko, Kvantovaya Elektronika **36**, 1131 (2006) [Quantum Electron. **36**, 1131 (2006)].
[8] K. C. Prince *et al.*, Nat. Photon. **10**, 176 (2016).
[9] N. Douguet, E. J. Gryzlova, E. I. Staroselskaya, K. Bartschat, and A. N. Grum-Grzhimailo, arXiv:1611.01878 (2016).
[10] P. Agostini, F. Fabre, G. Mainfray, G. Petite, and N. K. Rahman, Phys. Rev. Lett. **42**, 1127 (1979).
[11] P. Agostini, M. Clement, F. Fabre, and G. Petite, J. Phys. B: At. Mol. Phys. **14**, L491 (1981).
[12] P. Kruit, J. Kimman, and M. J. van der Wiel, J. Phys. B: At. Mol. Phys. **14**, L597 (1981).
[13] P. Kruit, J. Kimman, H. G. Muller, and M. J. van der Wiel, Phys. Rev. A **28**, 248 (1983).
[14] P. H. Bucksbaum, M. Bashkansky, R. R. Freeman, T. J. Mcllrath, and L. F. DiMauro, Phys. Rev. Lett. **56**, 2590 (1986).
[15] T. E. Glover, R. W. Schoenlein, A. H. Chin, and C. V. Shank, Phys. Rev. Lett. **76**, 2468 (1996).
[16] P. M. Paul, E. S. Toma, P. Breger, G. Mullot, F. Augé, Ph. Balcou, H. G. Muller, and P. Agostini, Science **292**, 1689 (2001).
[17] P. Radcliffe et al, Appl. Phys. Lett. **90**, 131108 (2007).
[18] P. O'Keeffe, R. López-Martens, J. Mauritsson, A. Johanson, A. L'Huillier, V. Véniard, R. Taïeb, A. Maquet, and M. Meyer, Phys. Rev. A **69**, 051401 (2004).
[19] O. Guyétand, M. Gisselbrecht, A. Huetz, P. Agostini, R. Taïeb, V. Véniard, A. Maquet, L. Antonucci, O. Boyko, C. Valentin, and D. Douillet, J. Phys. B: At. Mol. Opt. Phys. **38**, L357 (2005).
[20] M. Meyer, D. Cubaynes, D. Glijer, J. Dardis, P. Hayden, P. Hough, V. Richardson, E. T. Kennedy, J. T. Costello, P. Radcliffe *et al.*, Phys. Rev. Lett. **101**, 193002 (2008).
[21] M. Meyer, J. T. Costello, S. Düsterer, W. B. Li, and P Radcliffe, J. Phys. B: At. Mol. Opt. Phys. **43**, 194006 (2010).
[22] V. Richardson, W. B. Li, T. J. Kelly, J. T. Costello, L. A. A. Nikolopoulos, S. Düsterer, D. Cubaynes and M. Meyer, J. Phys. B: At. Mol. Opt. Phys. **45**, 085601 (2012).
[23] A. Maquet and R. Taïeb, J. Mod. Opt. **54**, 1847 (2007).
[24] A. Cionga, V. Florescu, A. Maquet, and R. Taieb, Phys. Rev. A **47**, 1830 (1993).
[25] R. Taïeb, V. Véniard, A. Maquet, N. L. Manakov, and S. I. Marmo, Phys. Rev. A **62**, 013402 (2000).
[26] O. Guyétand, M. Gisselbrecht, A. Huetz, P. Agostini, R. Taïeb, A. Maquet, B. Carré, P. Breger, O. Gobert, D. Garzella *et al.*, J. Phys. B: At. Mol. Opt. Phys. **41**, 051002 (2008).
[27] L. H. Haber, B. Doughty, and S. R. Leone, J. Phys. Chem. A **113**, 13152 (2009).
[28] L. H. Haber, B. Doughty, and S. R. Leone, Phys. Rev A **84**, 013416 (2011).
[29] B. Doughty, L. H. Haber, C. Hackett, and S. R. Leone, J. Chem. Phys. **134**, 094307 (2011).
[30] A. Sperl, H. Rietz, M. Schoenwald, A. Fischer, K. Simeonidis, and J. Ullrich, *Multiphoton Processes and Attosecond Physics* (Springer Proceeding in Physics **125**, edits: Kaoru Yamanouchi and Katsumi Midorikawa, 2012).
[31] S. Düsterer *et al*, J. Phys. B: At. Mol. Opt. Phys. **46**, 164026 (2013).
[32] S. Hutchinson, M. A. Lysaght, and H. W. van der Hart, Phys. Rev. A **88**, 023424 (2013).
[33] A. N. Grum-Grzhimailo and E. V. Gryzlova, Phys. Rev. A **89**, 043424 (2014).
[34] S. Düsterer *et al*, J. Phys. B: At. Mol. Phys. **49**, 165003 (2016).
[35] G. Hartmann *et al*, Rev. Sci. Instrum. **87**, 083113 (2016).
[36] T. Mazza *et al.*, J. Mod. Opt., **63**, 367 (2016).
[37] P. Lambropoulos, Adv. At. Mol. Opt. Phys. **12**, 87 (1976).
[38] E. Cornier and P. Lambropoulos, J. Phys. B: At. Mol. Phys. **28**, 5043 (1995).
[39] L. A. A. Nikolopoulos, Phys. Rev. A **73**, 043408 (2006).
[40] V. Véniard and B. Piraux, Phys. Rev. A **41**, 4019 (1990).
[41] Y. Komninos, T. Mercouris, and C. A. Nicolaides, Phys. Rev. A **86**, 023420 (2012).
[42] L. V. Keldysh, Sov. Phys. JETP **20**, 1307 (1965).
[43] F. H. M. Faisal, J. Phys. B: At. Mol. Phys. **6**, L89 (1973).
[44] H. R. Reiss, Phys. Rev. A **22**, 1786 (1980).
[45] H. R. Reiss Prog. Quantum Electron. **16** 1 (1992).
[46] A. K. Kazansky, A. V. Grigorieva, and N. M Kabachnik, Phys. Rev. A **85**, 053409 (2012).
[47] J. H. Bauer, J. Phys. B: At. Mol. Phys. **41**, 185003 (2008).
[48] J. H. Bauer, Phys. Rev. A **85**, 063417 (2012).
[49] A. N. Grum-Grzhimailo, E. V. Gryzlova, E. I. Staroselskaya, J. Venzke, and K. Bartschat, Phys. Rev. A **91**, 063418 (2015).
[50] A. K. Kazansky, A. V. Bozhevolnov, I. P. Sazhina, and N. M. Kabachnik, J. Phys. B: At. Mol. Phys. **47**, 065602 (2014).
[51] M. Jain and N. Tzoar, Phys. Rev. A **18**, 538 (1978).
[52] G. Duchateau, E. Cormier, and R. Gayet, Phys. Rev. A **66**, 023412 (2002).
[53] V. D. Rodríguez, E. Cormier, and R. Gayet, Phys. Rev. A **69**, 053402 (2004).
[54] D. G. Arbó, J. E. Miraglia, M. S. Gravielle, K. Schiessl, E. Persson, and J. Burgdörfer Phys. Rev. A **77**, 013401 (2008).
[55] A. K. Kazansky, I. P. Sazhina, and N. M. Kabachnik, Phys. Rev. A **82**, 033420 (2010).
[56] A. N. Grum-Grzhimailo, A. D. Kondorskiy, and K. Bartschat, J. Phys. B **39**, 4659 (2006).
[57] E. B. Saloman and C. J. Sansonetti, J. Phys. Chem. Ref. Data **33**, 1113 (2004).
[58] A. Kramida, Yu. Ralchenko, J. Reader, and NIST ASD Team (2015). NIST Atomic Spectra Database (ver. 5.3). Online available at `http://physics.nist.gov/asd`. National Institute of Standards and Technology, Gaithersburg, MD.
[59] L. E. Machado, P. L. Emerson, and G. Csanak, J. Phys. B: At. Mol. Opt. Phys. **15**, 1773 (1982).
[60] E. Cormier, D. Garzella, P. Breger, P. Agostini, G. Chériaux, and C. Leblanc J. Phys. B: At. Mol. Opt. Phys. **34**, L9 (2001).
[61] S. Xu, G. Sha, B. Jiang, W. Sun, X. Chen, and C. Zhang

J. Chem. Phys. **100**, 6122 (2001).
[62] S. E. Moody and M. Lambropoulos, Phys. Rev. A **15**, 1497 (1977).
[63] P. Kruit, J. Kimman, H. G. Muller and M. J. van der Wiel J. Phys. B: At. Mol. Opt. Phys. **16**, 937 (1983).